Mansoura Engineering Journal

Volume 48 | Issue 5 Article 13

December 2023

An Image Processing Technique for Studying the Flame Structure Using Single Shots of OH-PLIF Diagnostics

Hazem M. Al-Bulqini
Mechanical Power Engineering Department, Faculty of Engineering, Mansoura University, Egypt, h.albulqini@mans.edu.eg

El-Shafie B. Zeidan
Mechanical Power Engineering Department, Faculty of Engineering, Mansoura University, Egypt

Farouk M. Okasha
Mechanical Power Engineering Department, Faculty of Engineering, Mansoura University, Egypt

Mohy S. Mansour
Mechanical Power Engineering Department, Faculty of Engineering, Cairo University, Egypt

ORIGINAL STUDY

An Image-processing Technique for Studying the Flame Structure Using Single Shots of OH-PLIF Diagnostics

Hazem M. Al-Bulqini [a,*], El-Shafie B. Zeidan [a], Farouk M. Okasha [a], Mohy S. Mansour [b]

[a] Mechanical Power Engineering Department, Faculty of Engineering, Mansoura University, Egypt
[b] Mechanical Power Engineering Department, Faculty of Engineering, Cairo University, Egypt

Abstract

Laser diagnostic techniques have played a crucial role in enhancing our understanding of combustion processes. Among these techniques, Planar Laser-Induced Fluorescence (PLIF) using OH radicals has proven to be a powerful tool for investigating reaction zones, flame curvature, and flame surface density in diverse flame modes including premixed, non-premixed, and partially premixed flames. However, to fully harness the potential of experimental measurements and laser diagnostics in studying combustion processes, a comprehensive grasp of image-processing techniques and tools is essential for effectively analyzing captured images and extracting valuable information. In this study, we present a detailed algorithm that facilitates the conversion of qualitative single-shot OH-PLIF images into quantitative data regarding flame structure under different conditions, encompassing flame curvature, flame surface density, and flame front angle. This methodology outlines the sequential steps necessary for extracting physical properties from images. Furthermore, we showcase results obtained using this algorithm, using flames under varying conditions to validate its effectiveness, compare studied parameters across different flames, and demonstrate its applicability to a wide range of combustion processes. Otsu's method of thresholding provides more accuracy in detecting the reaction zone over a wide range of conditions. Also, the Gaussian smoothing method with a standard deviation value of $\sigma = 2$ provides the most suitable way of smoothing without removing valuable data. The comparison between different flames results in a higher value of zero curvature ($P(\kappa) = 3.25$) and lower values of flame front angle ($P(\theta)$~0) when the flame shape has a less turbulent nature and more vertical jet shape.

Keywords: Data processing, Flame curvature, Flame surface density, High-speed images

1. Introduction

Despite being an aging method of energy generation, combustion continues to be a prominent source of energy that plays a crucial role in various essential activities such as heating, transportation, and electricity generation. Its significance is expected to persist in the coming years. Many countries, particularly those with abundant fossil fuel resources, heavily rely on combustion for power generation, propulsion, and vehicular operation. Research efforts aimed at enhancing the efficiency and environmental friendliness of engines, gas turbines, and furnaces, as well as optimizing chemical processes and minimizing fire damage, have the potential to greatly enhance the quality of life worldwide. These advancements will not only improve competitiveness and sustainability but also have positive impacts on the environment, economy, and employment opportunities (Aldé et al., 2011).

To optimize and control combustion processes effectively, it is crucial to have measurement methods capable of capturing important factors such as temperature, species concentration, velocity, and particle properties. However, the complex nature of combustion, characterized by high temperatures,

Received 4 February 2023; revised 27 June 2023; accepted 3 July 2023.
Available online 8 December 2023

* Corresponding author. Mechanical Power Engineering Dept., Faculty of Engineering, Mansoura University, Elgomhoria St., Mansoura City 35516, Egypt.
E-mail address: h.albulqini@mans.edu.eg (H.M. Al-Bulqini).

https://doi.org/10.58491/2735-4202.3071

high pressures, turbulent gas flows, a wide range of fuels, and potential phase transitions, presents significant challenges in this field (Aldé et al., 2011). Fortunately, the advancement of laser diagnostic tools in recent decades has significantly enhanced our understanding of combustion processes through experimental progress. These nonintrusive techniques offer several advantages compared with other measurement methods, as they cause minimal noise and disturbance to the measured data. Laser diagnostics enable precise measurements while minimizing interference, allowing for more accurate analysis and control of combustion processes. Planar laser-induced fluorescence (PLIF) is widely recognized as a standard tool for visualizing the spatial distributions of temperature and various combustion intermediate products (Skiba et al., 2018a). In the study of turbulent flames, there has been a significant focus on depicting flame front positions and structures. Among the different species, measurements of OH dispersion have garnered the most attention due to its high concentration in flames and the synchronicity of OH transitions with the wavelengths emitted by powerful excimer lasers (Bockle et al., 2000). For this reason, many researchers considered this method in their work.

Accordingly, Gordon et al. (2008) used the PLIF technique to examine the stability of methane turbulent flames in a high-temperature vitiated co-flow system. Also, Frank et al. (2005) utilized PLIF diagnostics to acquire two-dimensional measurements of mixture fraction, temperature, scalar dissipation rate, and forward reaction rate in turbulent partially premixed flames with argon dilution. In their study, Li et al. (2010) designed a coaxial jet burner to generate turbulent flames and used concurrent single-shot PLIF imaging of CH, OH, and CH_2O to visualize the local flame front structure. Their objective was to investigate the influence of turbulence eddies on the structure of the reacting zone. Moreover, Kiefer et al. (2008) also used simultaneous single-shot OH and CH PLIF imaging to investigate the flame structure, with a particular emphasis on obtaining quantitative statistical data for different flames and calculating flame surface density.

Wabel et al. (2017) conducted a study using OH-PLIF diagnostics to qualitatively identify the flame regimes of premixed flames subjected to extreme turbulence levels. They specifically investigated the thickness of the preheated layer, the residence time of eddies in the flame, and the reaction layers in comparison to laminar values. Furthermore, numerous other researchers have adopted similar approaches to study flame structure under various conditions, using qualitative and quantitative methods based on their specific areas of investigation (Carter et al., 2014, 2016; Skiba et al., 2017, 2018b). To gain deeper insights into the reaction zone of premixed flames, heat rate measurements play a crucial role. Kariuki et al. (2015) conducted simultaneous OH- and CH_2O-PLIF imaging in premixed flames to obtain heat rate measurements. These measurements were obtained by multiplying the OH- and CH_2O-PLIF images on a pixel-by-pixel basis after a prolonged detection period. This approach builds upon the earlier

Nomenclature and symbols

B	Blue color value
CH	Methylidyne radical
CH_2O	Formaldehyde
CH_4	Methane
dA	Flame surface area, mm^2
dL	Infinitesimal flame front length, mm
dV	Flame volume, mm^3
G	Green color value
G(x, y)	Gaussian filter value
GRAYSCALE	Value of a certain point on the grayscale color model
H	Burner height, mm
HCO	Bicarbonate
i	Integer counter for successive points on a curve
l	Horizontal distance downstream the laser direction, mm
L/D	Dimensionless mixing length
max	Maximum value
min	Minimum value
OH	Hydroxyl radical
P	Arbitrary point
P(θ)	The Probability Density Function of a certain value of flame front angle
P(κ)	The Probability Density Function of a certain value of curvature
PLIF	Planar Laser-Induced Fluorescence
Q	The neighboring point to P
R	Red color value
r	Flame radius, mm
Re	Reynolds number
RGB	Red–green–blue color model
x	Horizontal spatial coordinates
$\dot{x}$	First derivative in the horizontal direction
$\ddot{x}$	Second derivative in the horizontal direction
y	Vertical spatial coordinates
$\dot{y}$	First derivative in the vertical direction
$\ddot{y}$	First derivative in the vertical direction
z/H	Dimensionless elevation above the burner tip
θ	Flame front angle
κ	Flame curvature, mm^{-1}
σ	Standard deviation
Σ	Flame surface density, mm^{-1}
Φ	Equivalence ratio

work of Najm et al. (1998), who established a correlation between the formyl radical HCO and heat release rates in laminar premixed flames. By using these techniques, researchers aim to gain a better understanding of the heat release processes occurring within premixed flames.

Therefore, all of the aforementioned experimental work necessitates a comprehensive approach that involves not only conducting the measurements but also utilizing image-processing techniques. Dealing with a large volume of single-shot images requires the extraction of relevant information by effectively handling noise reduction, addressing shot-to-shot variation, identifying areas of interest, performing calculations, and comparing results under different conditions. While many research papers primarily focus on presenting the results, their description, and comparisons, the importance of providing a solid reference for the necessary tips and tricks in handling this type of data and conducting one's experiments and analyses should not be overlooked. However, it is worth noting that these steps are often briefly outlined in the existing literature. As a result, new researchers may face challenges in acquiring a comprehensive understanding of the techniques involved in working with this type of data. For instance, the early work of Baldini et al. (Comelico and Milan, 2000) presented initial work demonstrating the application of image-processing techniques for combustion analysis, providing a brief overview of the methodology. Subsequently, Bayley et al. (2012) introduced a well-structured explanation of the image-processing algorithm they used to calculate flame curvature in a lean, partially premixed swirl-stabilized flame. Also recently, Wang et al. (2020) showcased in their paper a detailed image-processing algorithm for measuring flame stability in gas-fired combustion. Their study demonstrated the effectiveness of the algorithm in analyzing combustion phenomena and extracting valuable insights from the images obtained.

In addition, Wang et al. (2015) used high-speed schlieren/stereo imaging and image-processing techniques to investigate the ignition process of a methane diffusion-impinging flame. Boxx et al. (2013) developed an image-processing routine to autonomously identify and statistically characterize flame-kernel events using planar laser-induced fluorescence (PLIF) measurement. Besides, Darabkhani et al. (2013) used photomultipliers, high-speed photography, and digital image-processing techniques to study the structure of stable and unstable flame characteristics. Cui et al. (2021) studied a new image-based fire detection and processing technology using computer graphics, digital image-processing, and computer vision technology. Tachtatzis and Lu (2014) proposed an optimized image-processing technique to smooth flame contours for an improved accuracy in the measurement of the 3-D mean surface area ratio of a turbulent premixed flame. Moreover, Villani and Aquino (2020) reported the image acquisition process and the image processing necessary to evaluate the geometric characteristics of the propagating flame front. Shao (2007) used edge detection operators for flame image recognition and processing. Khalid et al. (2014) used optical visualization and image-processing techniques to determine the relation between mixture formation and flame development of burner combustion. Kim et al. (2015) investigated the variation of flame behavior, including the flame structure, using high-speed Schlieren photography and post-processing analysis of the high-speed images. Wang et al. (2018) applied special digital image-processing techniques to visualize the weak blue flame and weak yellow flame during the ignition process of a methane jet diffusion flame.

However, there are still gaps in the existing literature when it comes to image-processing algorithms for combustion analysis, primarily due to two main reasons. First, there is a lack of detailed explanations and step-by-step analysis of the algorithms used, leaving out crucial information about how to address challenges encountered after imaging. Second, there is a need for the development of a comprehensive algorithm that can be applied to a wide range of combustion physics, enabling the study of flame structure in terms of flame curvature, flame surface density, and flame front angle.

In this paper, we aim to fill these gaps by introducing a general algorithm for image processing in combustion analysis. Our algorithm will be presented in detail, providing guidance for upcoming researchers to quickly and comprehensively learn about image-processing techniques for combustion analysis. In addition, we will apply this algorithm to various OH-PLIF images at different physics and different types of fuels, conducting a statistical analysis of flame curvature and flame surface density. By comparing the results obtained under different flame conditions, we demonstrate the versatility of this algorithm for studying flames in diverse settings.

2. Methodology

Experimental setups are specifically designed to generate images of flames. One commonly used

technique for visualizing temperature and combustion intermediate products' spatial distributions is planar laser-induced fluorescence (PLIF) (Skiba et al., 2018a). Researchers have focused on studying flame front positions and structures in turbulent flames, with a particular emphasis on measuring the dispersion of OH due to its abundance in flames and its compatibility with excimer lasers that emit powerful wavelengths (Bockle et al., 2000). Consequently, many researchers have incorporated this approach into their studies. In the following subsection, we describe the implementation of the OH-PLIF system used to examine the structure of specific flames.

The setup comprises an Nd:YAG laser (Edgewave IS411-E) used for pumping a Rhodamine 6G dye laser (Sirah Credo) to generate an emission with a wavelength of 566 nm. Using a BBO crystal, the second harmonic generation (SHG) of the pumping wavelength (566 nm) produces an excitation wavelength of 283 nm. This particular wavelength is well suited for the $A^2\Sigma \leftarrow X^2\Pi$ (1,0) transition necessary to obtain the fluorescence signal. Laser sheet optics are used to transform the laser beam into a laser sheet measuring 1 mm in thickness and 100 mm in height. To capture the OH fluorescence signal, a LaVision high-Speed-Star 6 (HSS6) CMOS camera is used, operating at a frame rate of 10 kHz. The camera is equipped with a LaVision IRO lens-coupled two-stage intensifier, as well as a UG1-bandpass filter and a WG295-longpass filter. For more details about those experimental setups, a proper explanation can be found in (Mansour et al., 2017, 2020).

After generating images, each OH-PLIF image has to go through many steps in corrections. These corrections are as follows.

2.1. Laser beam inhomogeneity

The laser beam has an inhomogeneous distribution of energy most of the time due to many factors. For example, a part of laser energy is absorbed inside the reaction zone instead of exciting the OH radical, which leads to some gradient of error in signal in the downstream direction of the laser beam. If this error is not solved, misleading information about the local OH intensity results and gives low intensities in some regions due to the energy absorption not due to real low values of OH intensity. So, we need to know the gradient by which the laser energy is absorbed and remove its effect from images, so we can reproduce the real values of OH radical in the generated images. We deal with each image as a 2D matrix, and each cell of the matrix has a certain value that represents the local OH intensity at that position. So, we use MATLAB software to deal with images and make our corrections and calculations. Hence, for a large dataset of n images, we create a 3D matrix of dimensions x, y, and n, where x and y are the number of rows and columns of each image (the number of pixels) and n the number of images in a dataset. And for determining the gradient error of the laser beam, we make a single 2D matrix in which we calculate average values of OH intensities at each cell/pixel. In this averaged image, we can notice how the laser beam deviates from being homogeneous across the reaction zone, and we can extract a gradient by which the laser energy is absorbed. So, we apply the reverse of this gradient to every single image of the dataset, modifying the values of OH intensities and bringing them back as there is no energy absorption in the reaction zone. Fig. 1 shows the difference between the laser beam profile before correction due to absorption and the modified one. A quantitative method to show the difference is to take three vertical profiles at three different horizontal positions downstream of the direction of the laser beam (the right direction) to illustrate how the laser intensity decreases in the horizontal direction. This can be noticed by the reduction in the peak value for each profile (Fig. 1c and d).

Another sort of inhomogeneity is the natural distribution of the laser sheet, from having a maximum value (around 1) at the center of the sheet, and this value decreases above and below the centerline. This distribution also gives incorrect values of the resulted OH intensity at the top and the bottom of the images, leading to correct values of OH radical in the middle of images and lower values at the sides. This also needs to be modified by normalizing each image by this Gaussian profile of the laser beam. So, if the values in the middle of the images are divided by values ~1, this gives almost the same value, but when the pixels are divided by values below 1. This increases their local values and gives the real intensity of OH radical at those regions. Fig. 2 shows an example of a single image from Ref (Mansour et al., 2020). before and after modification.

2.2. Smoothing

For images to represent real flames, an accurate smoothing of each image has to be done. This smoothing should eliminate the so-called 'salt and pepper' noise in images and also should preserve the real shape of the flame front. When compared with the traditional filters now in use, smoothing images with a 2D Gaussian filter produces the greatest results (Tyagi and Mishra, 2016). A 2D

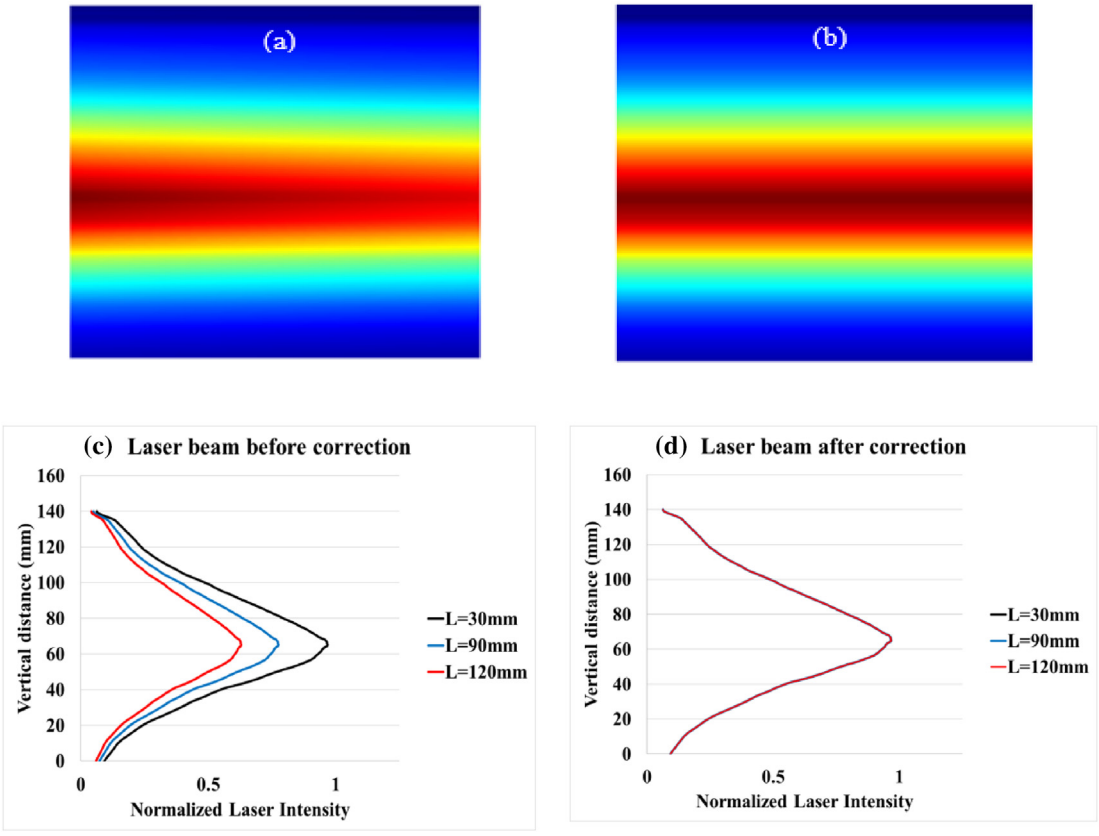

Fig. 1. (a, c) Beam profile before correction and (b, d) beam profile after correction.

convolution operator called the Gaussian smoothing operator is used to 'blur' images and eliminate noise and detail. It is comparable to the mean filter (which reduces the intensity value variation between one pixel and the neighboring) in this regard, but it makes use of a different kernel that simulates a Gaussian (or 'bell-shaped') hump. In 2D, an isotropic (i.e. circularly symmetric) Gaussian has the form

$$G(x,y)=\frac{1}{2\pi\sigma^2}e^{-\frac{x^2+y^2}{2\sigma^2}} \quad (1)$$

where G (x, y) is the value of the Gaussian filter; σ is the standard deviation; and x and y are the spatial coordinates.

This distribution is shown in Fig. 3.

To achieve the result of proper smoothing, changing the value of standard deviation plays a key

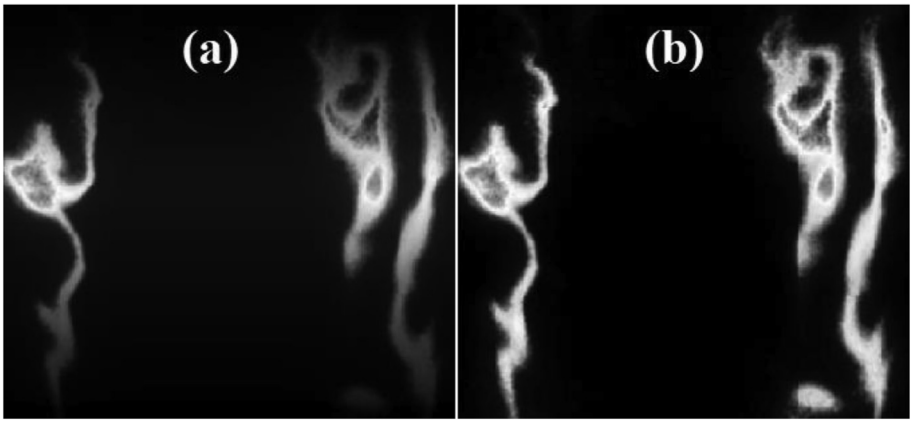

Fig. 2. A comparison of the flame from Ref (Mansour et al., 2020): (a) before modification and (b) after modification.

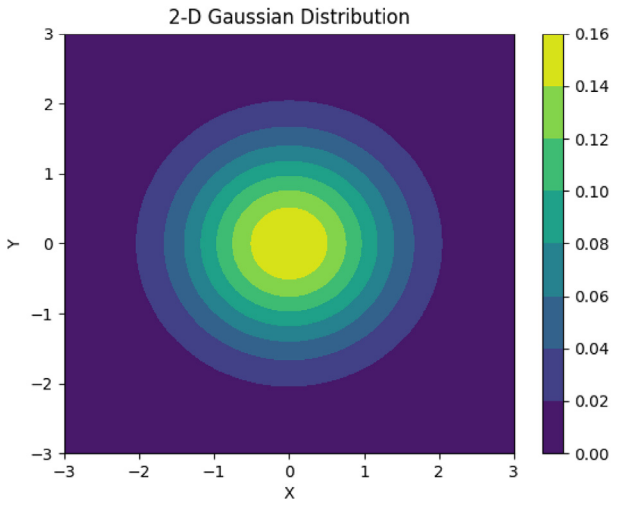

Fig. 3. 2-D Gaussian distribution with mean (0, 0) and σ = 1.

role in this aspect. So, we need to try and see until the resulting images reach a satisfying form.

Fig. 4 shows the comparison between different values of σ in the Gaussian filter and how it affects the resulting image. It is proved that a value of σ = 2 gives the best smoothing result to maintain the shape of the flame front to remove the unwanted noise in the image.

2.3. Grayscaling and thresholding

A color model is an abstract mathematical representation of how colors can be expressed as sets of three or four numerical values, or color components. The resulting collection of colors is known as 'color space' when this model is coupled with a clear description of how the components are to be interpreted, taking into consideration the visual perception (Hirsch, 2005). One of the most used color models is RGB. RGB is a model in which the red, green, and blue primary colors of light are added together in various ways to reproduce a broad array of colors. The name of the model comes from the initials of the three additive primary colors, red, green, and blue (Fairman et al., 1997). Digital cameras adapt this color model for producing images. So, for the OH single shots we have: each pixel of each image has a combination of three colors to represent the value of the pixel and to identify its color. A color is specifically described using three integer values for red, green, and blue that range from 0 to 255. A value of zero denotes darkness, while a value of 255 denotes brightness. When we combine these three primary colors, weighted by their values, the final color is determined by the values. White is produced by mixing all three colors equally (RGB = (255, 255, 255)), while black is produced by not using any colors at all (RGB = (0, 0, 0)). We can see all the various colors that the model can describe in the RGB coordinate system shown in Fig. 5.

So, the simplest model is grayscale because it just uses one component to define color, namely lightness. A value between 0 (black) and 255 is used to define the degree of brightness (white). However, images in grayscale provide less information than those in RGB. However, they are frequently used in image processing because doing so is quicker and uses less space when dealing with complex computations. The ways to convert RGB into grayscale are different. One of them is the lightness method. A very simple method is to take the average value of the components with the highest and lowest RGB values:

$$Grayscale = \frac{\min(R,G,B)+\max(R,G,B)}{2} \tag{2}$$

Since one RGB component is not utilized, it is clear that this approach has a severe flaw. The degree of lightness that our eyes detect depends on all three primary colors, thus this is unquestionably a problem. Another approach is to use the average of the red, green, and blue components as the grayscale value:

$$Grayscale = \frac{R+G+B}{3} \tag{3}$$

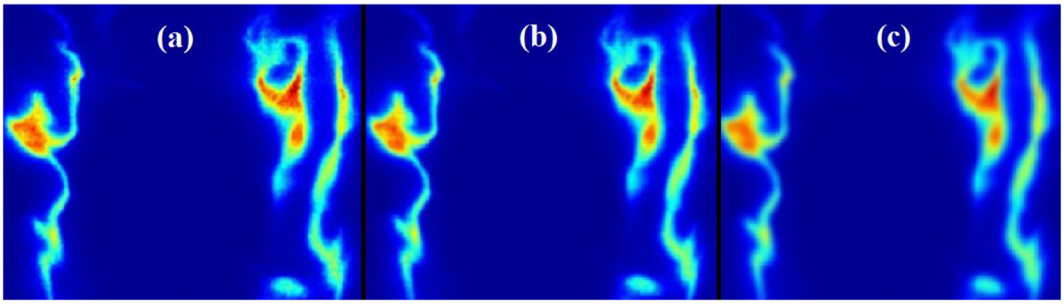

Fig. 4. Single shot from (Mansour et al., 2020) after smoothing by the Gaussian filter of (a) σ = 1, (b) σ = 2, and (c) σ = 5.

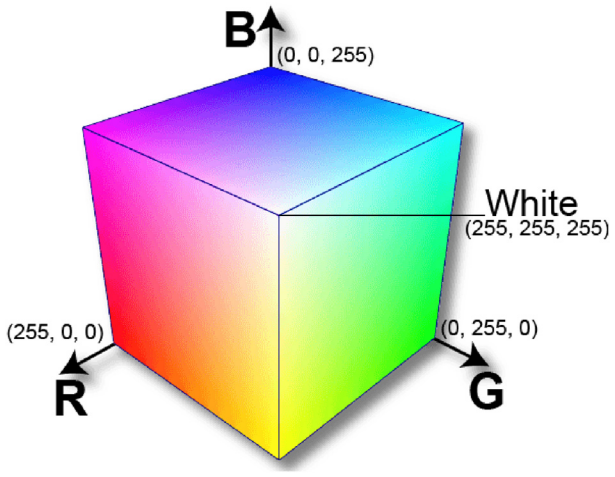

Fig. 5. A coordinate illustration of the RGB color model.

Although we now consider all components, the average technique is equally flawed because it gives each component the same weight. We know that our eyes respond to each color differently based on a study on human eyesight. In particular, green, red, and blue are the colors that our eyes are most sensitive to. As a result, the weights in the equation above should be adjusted. The luminosity method, which effectively addresses the shortcomings of earlier approaches, is the best approach. We should compute a weighted average of the components in light of the aforementioned findings. The final number should have a smaller percentage of blue and a larger percentage of green. Researchers have concluded the equation below after some trials and a more thorough analysis:

$$Grayscale = 0.3*R+0.59*G+0.11*B \quad (4)$$

Consequently, each pixel now has a single accurate value instead of 3 different values.

Now, each image is converted into grayscale with each pixel assigned a single value, so the next step now is to determine a value for thresholding in order to binarize the image into pixels of only two values: zero for no reaction zone and 1 for reaction zone contours. The method of thresholding should be accurate so the details of the flames do not vanish after thresholding in addition to excluding the very low intensities that mostly represent the noise in the images or very low OH radical intensity that should not be considered for further calculations. Lots of papers such as those of (Juddoo and Masri, 2011 and Cantu et al., 2016) make a threshold value by establishing a general threshold for the magnitude of the OH signal. This could be accurate for some cases, but to ensure that neither important details are ignored, nor noisy signals are considered, a more dynamic way of thresholding should be applied to the images, especially when they are a large amount covering many conditions. This is also in favor of the generality of the image-processing technique we previously mentioned. Hence, Otsu's method of thresholding (Otsu, 1979) is considered a suitable method for that purpose. Automatic image thresholding is carried out with Otsu's technique. The algorithm returns a single intensity threshold, dividing pixels into the foreground and background classes. This threshold is established by maximizing interclass variation or, alternatively, minimizing intra-class intensity variance. Fig. 6 shows the steps of thresholding and detecting the flame front contour.

2.4. Calculations

After extracting, in order, the points representing flame front contours from each single image of the data, it becomes available to do any calculations for the different flames. In this subsection, we will discuss the calculations done on the flame front contours to obtain informative results of flame curvature and flame surface density.

2.4.1. Flame curvature

The curvature, as the name suggests, is the deviation of a curve from a straight line. The flame front

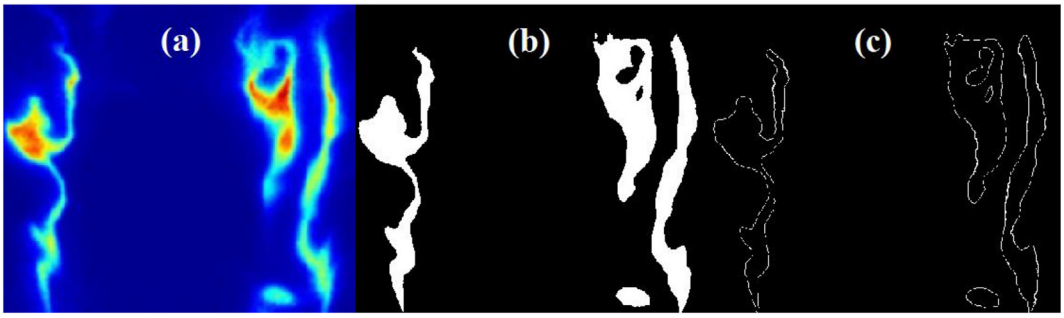

Fig. 6. (a) Single shot from Ref (Mansour et al., 2020). before thresholding, (b) after thresholding by Otsu's method, and (c) flame front capturing.

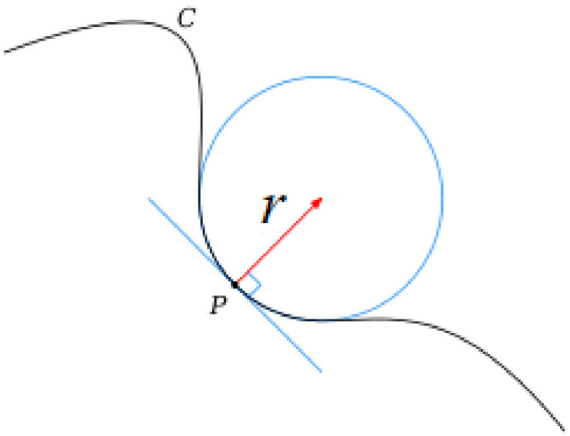

Fig. 7. An illustration of how an oscillating circle with a radius r resembles the curve C at a given point P.

is considered a differentiable curve as it is a continuous varying irregular line. So, to calculate the curvature for a flame front contour, we should use the oscillating circle method at each point of the contour. The oscillating circle is the circle which at a given location, most closely resembles the curve. To put it more properly, given a point P on a curve, each subsequent point Q forms a circle (or occasionally a line) that passes through Q and is perpendicular to the curve at P. If this circle has a limit when Q goes to P, it is the osculating circle, see Fig. 7. The center and radius of the osculating circle are then the center and radius of the curve at P. The reciprocal of the radius of curvature is the curvature. In other words, the curvature is defined as

$$\kappa = \frac{1}{r} \tag{5}$$

where r is the radius of curvature.

Equation (4) turns into this parametric representation of a twice differentiable plane curve according to the following equation (Kheirkhah and Gülder, 2013):

$$\kappa_i = \frac{\dot{y}\ddot{x} - \dot{x}\ddot{y}}{(\dot{x}^2 + \dot{y}^2)^{\frac{3}{2}}} \tag{6}$$

where x and y are the horizontal and vertical coordinates of the point on the flame front contour, respectively, whereas $(\cdot)$ and $(\cdot\cdot)$ represent the first and second derivatives, respectively. The curvature (κ_i) at any x and y can be estimated by the discretization of the previous equation as follows (Lomax and Polliam, 1999):

$$\kappa_i = \frac{8\left[x_{i-1}(y_{i+1} - y_i) + x_i(y_{i-1} - y_{i+1}) + x_{i+1}(y_i - y_{i-1})\right]}{\left[(x_{i+1} - x_{i-1})^2 + (y_{i+1} - y_{i-1})^2\right]^{\frac{3}{2}}} \tag{7}$$

It is important to keep in mind that κ_i has positive values when the curvature is convex toward the reactants' region and negative values when the curvature is concave. Along the flame edge, curve-fitting is performed. By carefully choosing the appropriate interval length during the curve-fitting procedure, oversampling and undersampling were avoided (Soika et al., 2003).

The LaVision high-Speed-Star 6 (HSS6) CMOS camera has an uncertainty of 2.8 electrons per pixel (LaVision). This indicates that there is a 2.8% probability of a pixel displaying a value different from its actual value. Several factors contribute to this uncertainty, including noise from the camera sensor, readout noise, and quantization noise. The sensor noise results from the random movement of electrons within the sensor, while readout noise stems from the electronic circuits responsible for retrieving the signal from the sensor. In addition, quantization noise arises from rounding the signal to a finite number of bits. So, to determine the uncertainty of κ_i when the variables x_i, y_i, x_{i-1}, y_{i-1}, x_{i+1}, and y_{i+1} have an uncertainty of 2.8%, we can use error propagation principles.

Let's assume that Δx_i, Δy_i, Δx_{i-1}, Δy_{i-1}, Δx_{i+1}, and Δy_{i+1} represent the uncertainties (expressed as a percentage) for their respective variables. Given that the uncertainties are all 2.8%, we can substitute $\Delta x_i = \Delta y_i = \Delta x_{i-1} = \Delta y_{i-1} = \Delta x_{i+1} = \Delta y_{i+1} = 2.8\% = 0.028$.

Using error propagation, the uncertainty of κ_i ($\Delta\kappa_i$) can be estimated as follows:

$$\Delta\kappa_i = |\partial\kappa_i/\partial x_i| * \Delta x_i + |\partial\kappa_i/\partial y_i| * \Delta y_i + |\partial\kappa_i/\partial x_{i-1}| * \Delta x_{i-1} + |\partial\kappa_i/\partial y_{i-1}| * \Delta y_{i-1} + |\partial\kappa_i/\partial x_{i+1}| * \Delta x_{i+1} + |\partial\kappa_i/\partial y_{i+1}| * \Delta y_{i+1}$$

To simplify the equation, let's consider that x_(i+1) - x_(i-1) and y_(i+1) - y_(i-1) are constants denoted as A1 and A2, respectively.

After evaluating the partial derivatives of κ_i with respect to each variable and substituting the uncertainties, we obtain

$$\Delta\kappa_i = 8 * (A_2/A_1) * 0.028 * [(A_1^2+A_2^2)^{1.5}]^{-0.5}$$

Simplifying further

$$\Delta\kappa_i = 0.224 * (A_1^2+A_2^2)^{-0.5}$$

Therefore, the uncertainty of κ_i, when x_i, y_i, x_{i-1}, y_{i-1}, x_{i+1}, y_{i+1} have an uncertainty of 2.8%, is given by the equation $\Delta\kappa_i = 0.224 * (A_1^2 + A_2^2)^{-0.5}$, where $A_1 = x_{i+1} - x_{i-1}$ and $A_2 = y_{i+1} - y_{i-1}$.

2.4.2. Flame surface density

The flame surface density (Σ) is estimated based on this assumption (Kiefer et al., 2008; Soika et al., 2003):

$$\Sigma = \frac{dA}{dV} = \frac{dL}{dA} \tag{8}$$

where dL, dA, and dV are the infinitesimal flame front length in dA, flame surface area in dV, and volume, respectively. An interrogation box area assigned for Σ calculations is made movable all along the flame front contour and we calculate the arc length dL inside this box at each point. So, high values of Σ representa more wrinkled flame at this position and also represent how the flame spreads and oscillates in time within the reaction zone.

Fig. 8 shows in conclusion how the algorithm work from the start of the corrected images to finally calculate the required parameters.

3. Results and discussion

In this section, we present the studied parameters that our algorithm can detect and calculate for flame at different conditions. These parameters are flame curvature, flame surface density, and flame front angle. These parameters are selected for their importance for combustion. For instance, by

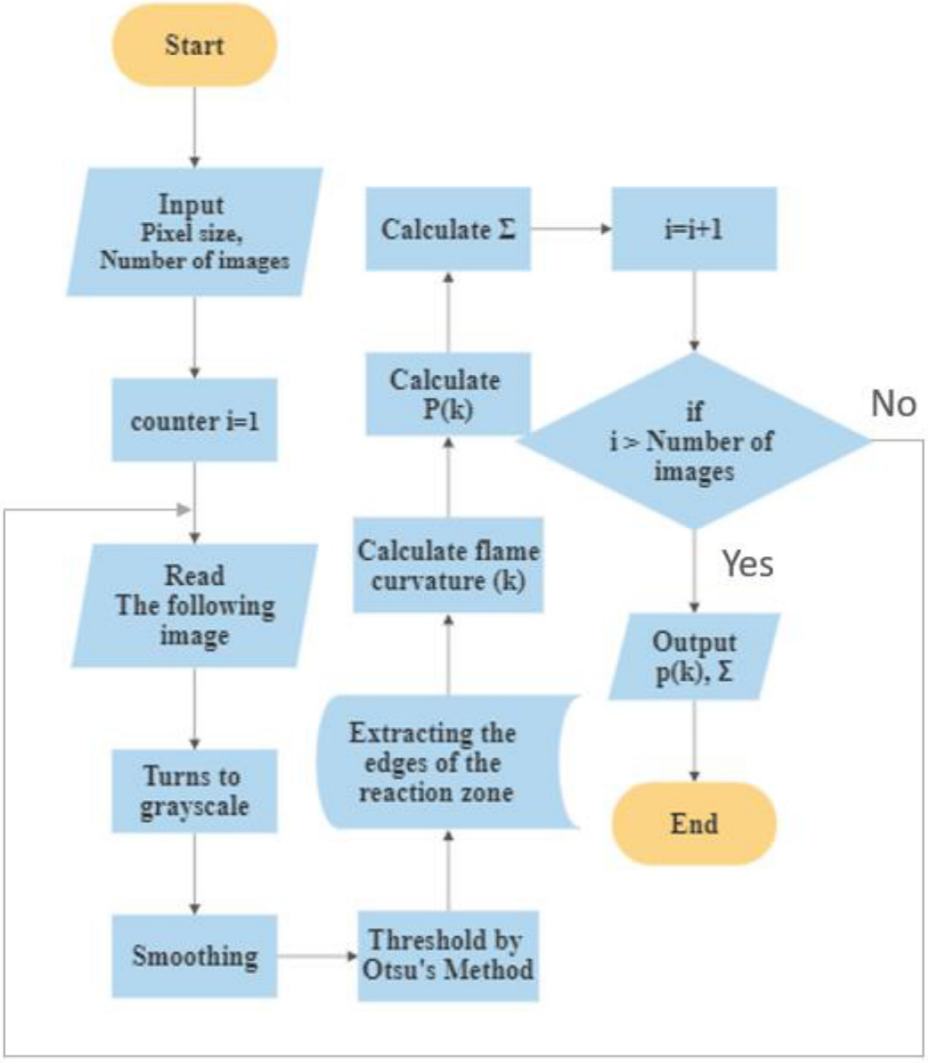

Fig. 8. A flowchart of the image-processing algorithm.

examining the curvature, researchers can understand the influence of factors such as burner geometry, flow conditions, and combustion properties on the shape and structure of the flame. This information is crucial for optimizing combustion systems, improving fuel efficiency, and reducing emissions. In addition, flame curvature affects the stability and propagation characteristics of the flame, making it essential to study safety considerations in applications such as engines, furnaces, and turbines. Flame surface density is an important parameter that indicates the degree of flame wrinkling and mixing. Higher flame surface density suggests greater interaction between the fuel and the oxidizer, leading to enhanced combustion efficiency and heat release. And flame front angle provides insights into the flame propagation characteristics, turbulent flow interactions, and combustion behavior. It helps in understanding how the flame interacts with different flow patterns, obstacles, or confinement within combustion systems.

3.1. Flame curvature

To verify the proposed algorithm, we applied this technique to five cases of OH-PLIF images of flames at different conditions from the literature. Figs. 9–14 show the selected single shots we chose to apply the algorithm on and to compare their results. Flames a, b, and c are CH_4 flames, flame d is for ammonia, flame (e) is hydrogen flame, and flame (f) is propane. This variety helps in selecting fuel types to further validate the generality of our algorithm and to cover a wider range of cases. Table 1 indicates the properties of used fuels.

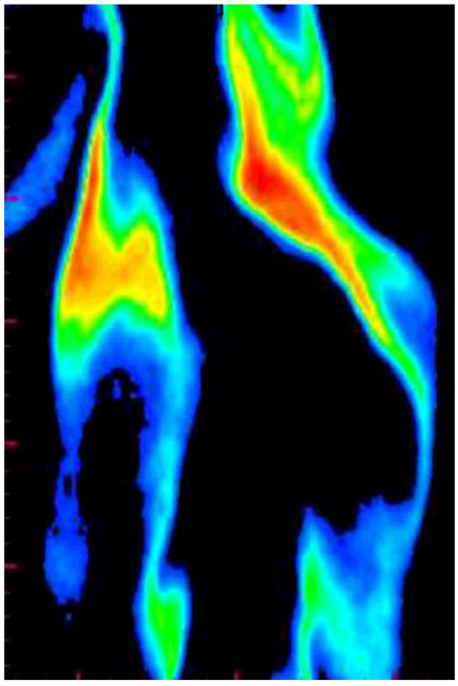

Fig. 9. OH field of partially premixed turbulent flame in concentric flow conical burner at L/D = 7, Φ = 2, Re = 10000 (flame (a)) (Mansour et al., 2017).

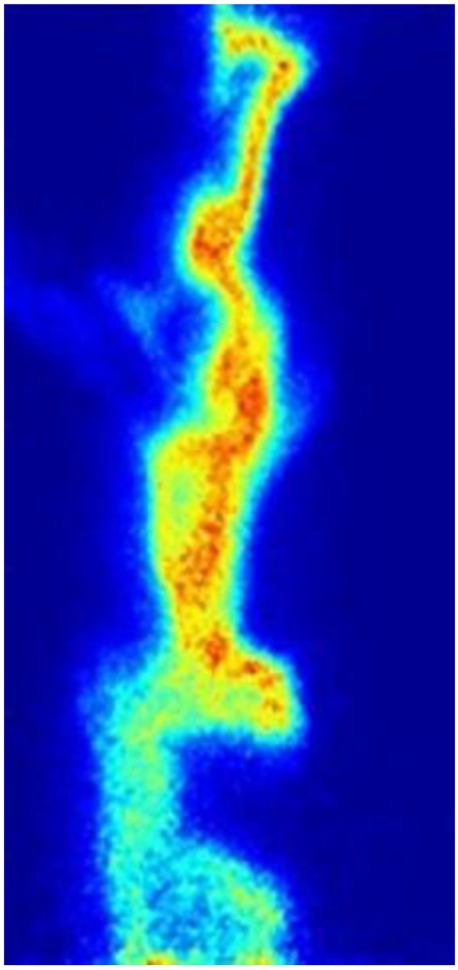

Fig. 10. OH field of partially premixed turbulent flame in concentric flow slot burner at L/D = 7, Φ = 2, Re = 10000. (flame (b)) (Mansour et al., 2020).

For all of the flames, the flame front has been detected and flame curvature κ has been calculated at each point, and to easily compare the different cases, a statistical analysis has been made to evaluate the frequency by which a certain value of κ has appeared. So, a probability density function of curvature P(κ) has been calculated for each flame and a comparison of them has been made in Fig. 15. Zero values of κ indicate a straight line at a certain position on the flame front. In other words, κ = 0 and the high value of P (0) mean less wrinkled flames. As shown in Fig. 9, flame (a) shows less wrinkled

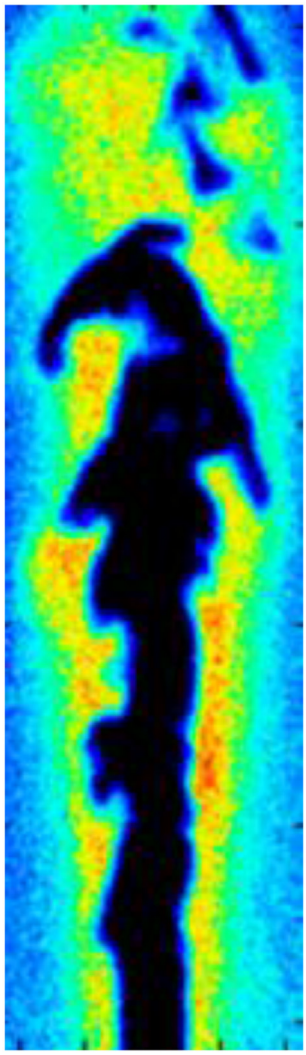

Fig. 11. OH field of premixed turbulent flame in a circular burner at Φ = 0.9, dilution of N_2 = 30%, Re = 6000. (flame (c)) (Yang et al., 2020).

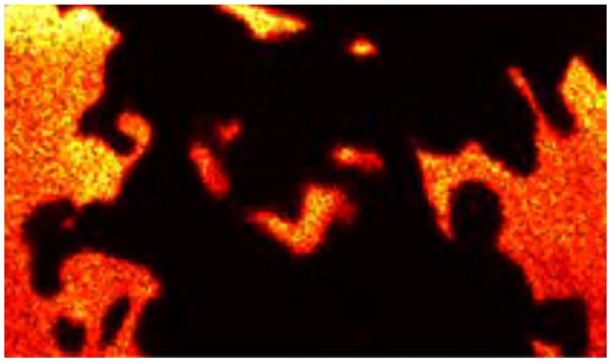

Fig. 12. OH field of premixed ammonia/air turbulent flame at Φ = 1, Re = 892 (flame (d)) (Fan et al., 2022).

flames with a high value of P (0) compared with flame (b), and this, in turn, shows the effect of burner geometry on flame curvature as both flame (a) and (b) are partially premixed under the same conditions of mixing length L/D, equivalence ratio Φ, and Reynolds number Re.

A more wrinkled flame with lower value of P (0) is shown in flame (c), and much more wrinkled flames with lower values of P (0) are shown in flames (d,e). And these results agree with the shapes of the OH fields shown in Figs. 9–13, while more flame kernels and flame separations appear obviously in the OH fields. This is mostly due to the burner nature of flame (e) as the combustion occurs in a cavity-based scramjet combustor. Another important factor to link between the cases is the equivalence ratio. A higher equivalence ratio leads to less curvature regardless of the fuel type, and this is very clear in (a,b) compared with flame (e), which indicates the effect of this parameter on flame structure.

To further investigate the flame curvature, we have also studied how the curvature changes downstream of the burner jet. We divided the area downstream of the burners into three zones and calculated the average κ within each zone to see how the average value of curvature changes in the downstream direction. We defined a dimensionless parameter z/H, where z is the height of the zone above the burner and H is the total height of the image. Fig. 16 shows how the absolute value of the average curvature changes at different z/H.

It is noticeable that the average curvature increases as the flame propagates downstream as the natural behavior of jet flows tends to have more eddies and vortices downstream the jet stream, which leads to a higher curvature. Also, we can notice similar trends with the results of P(κ) as flame (a) has overall lower curvature values compared with (b) and (c) while much higher curvature values resulted in flames (d,e) due to the separation and higher turbulent nature of the flames.

3.2. Flame surface density

Flame surface density Σ has also been calculated for the selected flames. Fig. 17 illustrates the value of Σ at each position on the flame front contour. More qualitative information about the flame surface density shall appear when comparing the selected flames by a set of images over a period of time to show how the flames spread and widen at different conditions, but this figure also indicates the accuracy of flame front selection, which in turn validates the image-processing technique which is the core of this article.

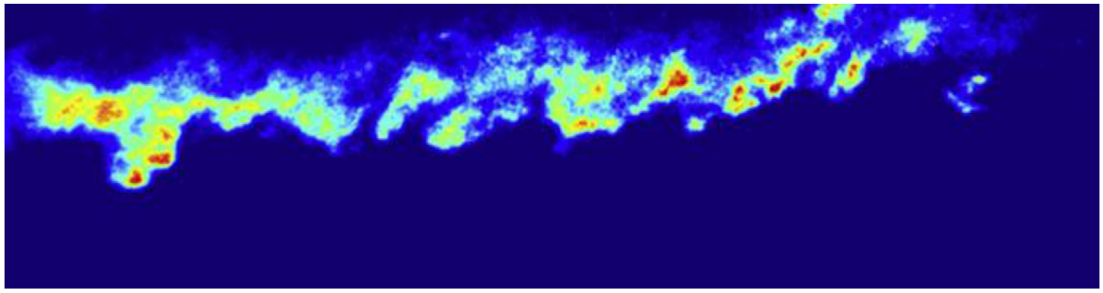

Fig. 13. OH field of premixed hydrogen turbulent flame at Φ = 0.3 (flame (e)) (Gao et al., 2022).

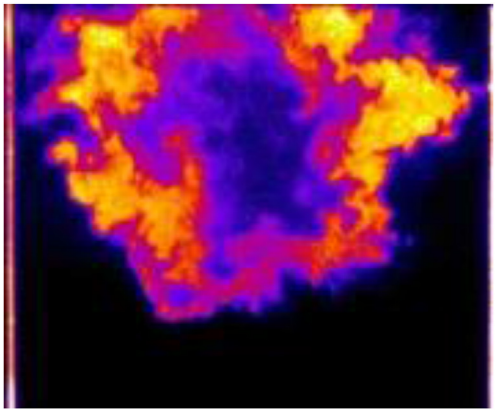

Fig. 14. OH field of premixed Hydrogen turbulent flame at Φ = 0.18 (flame (f)) (Johansen et al., 2014).

3.3. Flame front angle

As illustrated in Fig. 18, the angle between the vertical axis and the normal vector to the flame front toward the unburned zone is used in this study to evaluate the local flame front angle. Researchers (Tamadonfar and Gülder, 2015; Zhang et al., 2014) earlier used a similar definition for premixed turbulent flames. It was established that the local flame front angle is positive (negative) when it is moving in the counter-clockwise (clockwise) direction.

The local flame front angle gives additional information to the curvature as it describes the direction and orientation of the flame front. Fig. 19 illustrates the probability density functions' P(θ) curves for the local flame front angle of all flames of this study.

The figure shows that flame (c) has a more symmetric profile of P(θ) around the zero value, which means that it has nearly similar local flame front angles along the flame front. And this agrees with its OH field image in Fig. 11. However, due to the local tilting of flames (a) and (b) and the local reaction zones and kernels of these cases for being partially premixed, their curves of P(θ) tend to be less symmetric, which as previously mentioned can add to the information provided by P(κ) about the flame front and its propagation. As for flames (d,e), they

Table 1. Properties of fuels.

Fuel	Property	Value
Methane	Viscosity (μ. Pa.s) @ 300 K (Izzaty et al., 1967)	11.1
	Diffusion coefficient (Torr.cm^2.s^{-1}) @ 298 K (Tang et al., 2015)	168 ± 5
	Heating value (MJ/kg) (McAllister et al., 2011)	55.5
	Molecular weight (kg/kmole)	16
	Density (kg/m^3) @ 20 °C (Steven et al., 2000)	0.668
Ammonia	Viscosity (μ. Pa.s) @ 300 K	10.07
	Diffusion coefficient (Torr.cm^2.s^{-1}) @ 298 K (Spiller, 1989)	0.228 ± 0.012
	Heating value (MJ/kg) (Valera-Medina et al., 2018)	18.8
	Molecular weight (kg/kmole)	17.031
	Density (kg/m^3) @ 20 °C	0.73
Hydrogen	Viscosity (μ. Pa.s) @ 300 K	9.92
	Diffusion coefficient (Torr.cm^2.s^{-1}) @ 298 K	0.19
	Heating value (MJ/kg)	120.1
	Molecular weight (kg/kmole)	2.016
	Density (kg/m^3) @ 20 °C	0.08
Propane	Viscosity (μ. Pa.s) @ 300 K (Propane)	8
	Diffusion coefficient (Torr.cm^2.s^{-1}) @ 298 K	0.189
	Heating value (MJ/kg)	46
	Molecular weight (kg/kmole)	44.097
	Density (kg/m^3) @ 20 °C	2.005

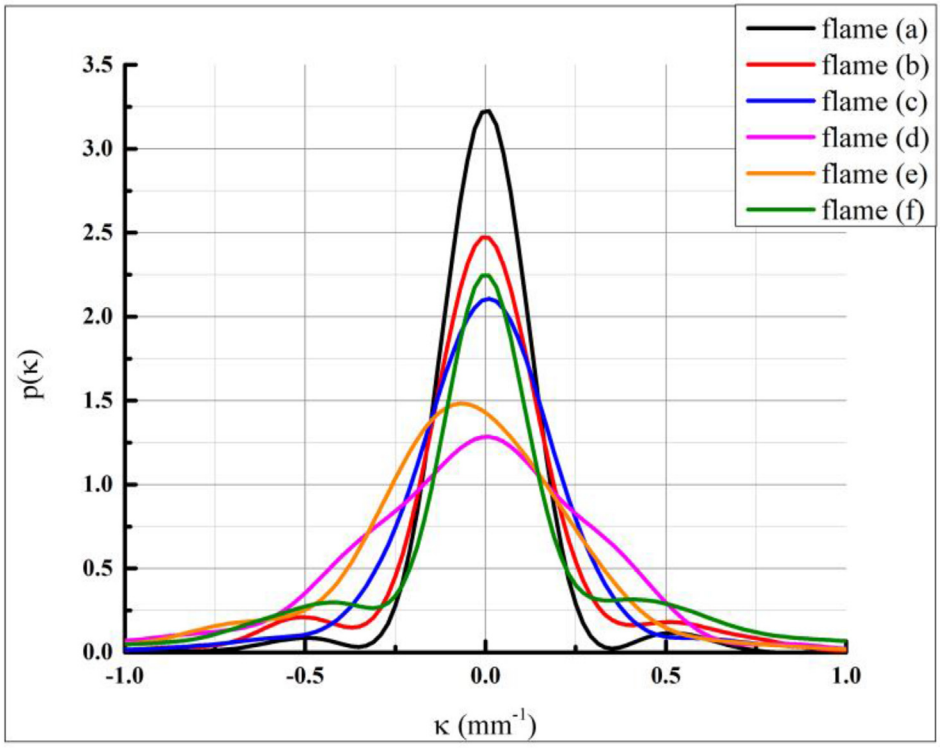

Fig. 15. Probability density function of flame curvature of selected flames.

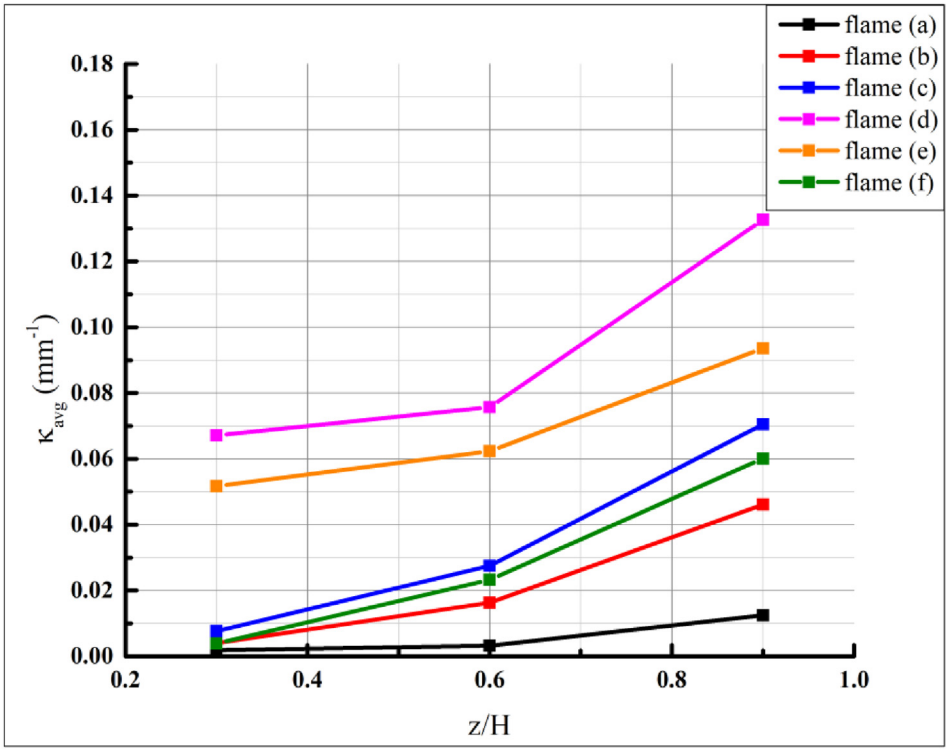

Fig. 16. Behavior of the average curvature downstream of the burner exit for flames (a), (b), (c), (d), (e), and (f).

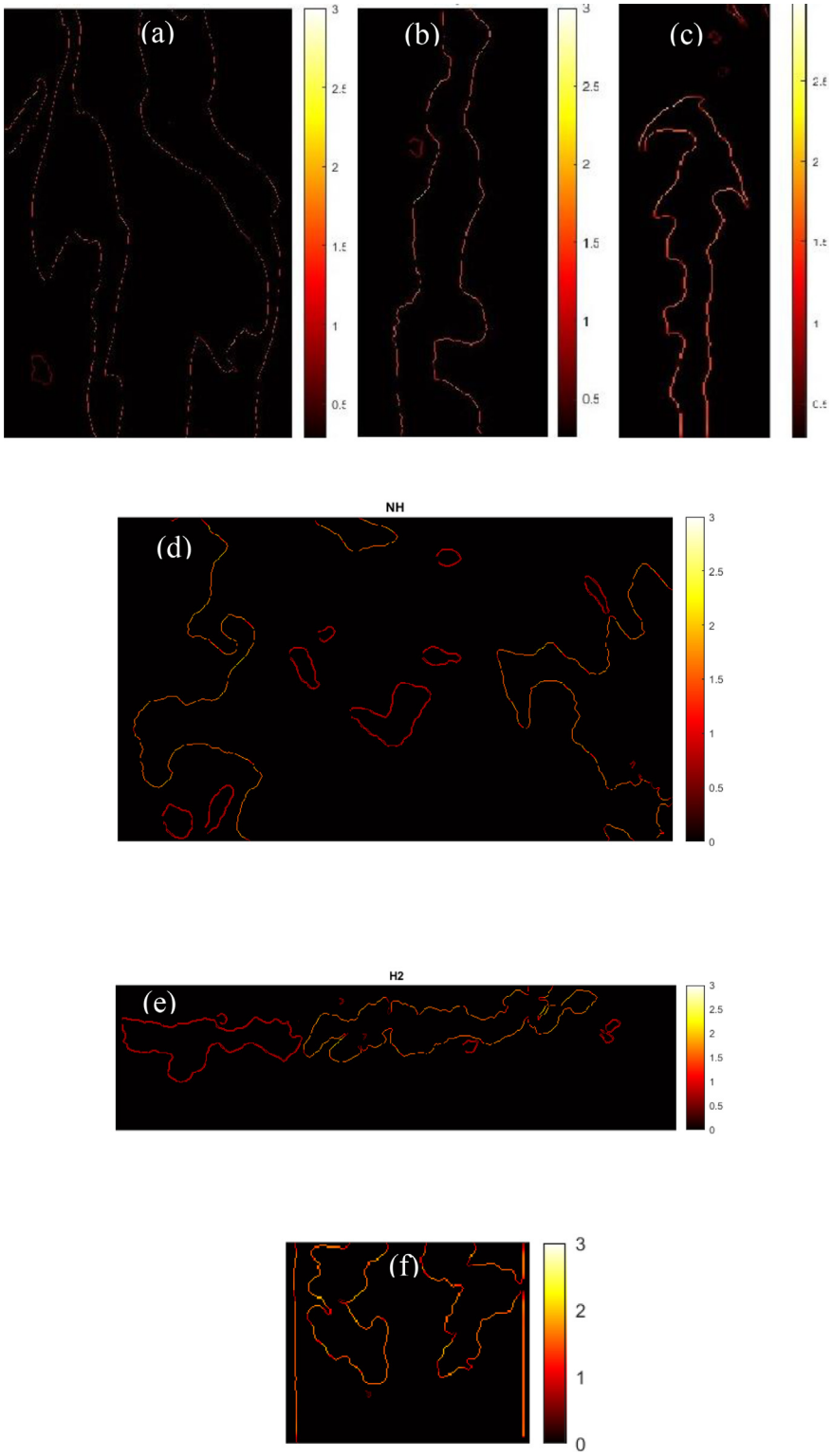

Fig. 17. The flame surface density values at their local position for the selected flames.

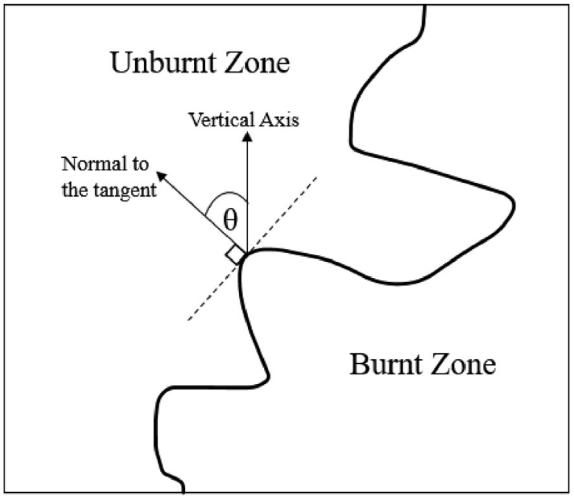

Fig. 18. The local flame front angle definition (Tamadonfar and Gülder, 2015).

have different nature from the other flames due to the burner geometry and fuel types. The flames do not have the axial symmetric shape as a flame (a,b,c and f), so the flame front angle profiles give a different trend from the other flames with higher values of $P(\theta) = 0$ as the flames tend to be horizontal at many positions in the OH field images.

3.4. Conclusion

A detailed algorithm dealing with each step of image processing from being raw data of images with noise and error to having valuable quantitative data of flame structure has been developed and illustrated. To validate this algorithm, a wide range of flame conditions has been tested and covered in this study from premixed to partially premixed conditions and with more than one fuel type. And the results of this work can be concluded as follows:

(1) The study of flame structure can greatly benefit from the application of image-processing techniques.
(2) To avoid misleading results, it is crucial to consider various correction factors.
(3) The Gaussian filtering method is a powerful tool for image smoothing, particularly with standard deviation values of around 2.
(4) Otsu's thresholding method is a more reliable approach for dynamic thresholding compared with using a single value in different cases.
(5) This algorithm demonstrates its versatility by effectively working with both premixed and partially premixed flames.

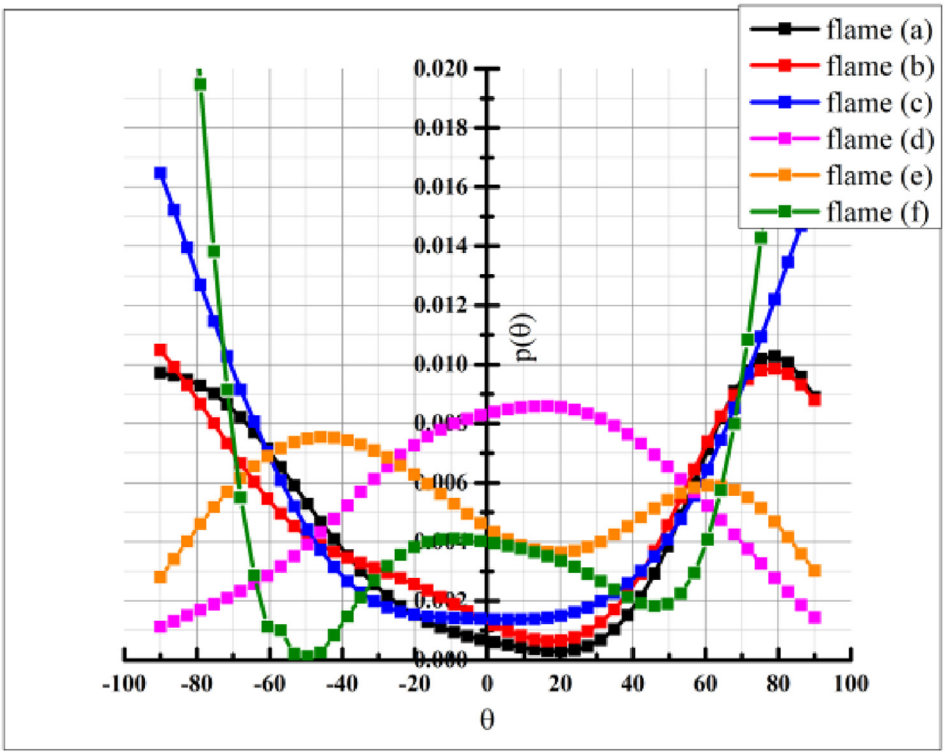

Fig. 19. Probability density functions' curves of the flame front angle θ for flames (a), (b) (c), (d), (e), and (f).

(6) The geometry of the burner impacts the curvature of the flame, as observed when comparing flame (a) to flame (b).
(7) Despite a relatively lower Reynolds number (Re), premixed conditions exhibit more wrinkled flames compared with partially premixed conditions.
(8) The equivalence ratio (Φ) has a significant effect on flame curvature. Lower values of Φ lead to more winkled flames and higher values of curvature regardless of the fuel type.
(9) Curvature tends to increase downstream as the flame propagates due to the formation of eddies and the dispersion of the flow.
(10) Flames (d, e) have higher values of curvature and flame surface density due to the wrinkled nature of the flames and lower values of Φ.
(11) Flames (c, d, e) show a higher flame surface density, indicating increased wrinkling.
(12) The local flame front angle adds valuable information about the flame front orientation with more symmetric probability for the premixed flames compared with the partially premixed ones.

Author credit statement

Hazem M. Al-Bulqini: Study conception, Writing – original draft, Data analysis and interpretation, Methodology, Visualization. **El-Shafie B. Zeidan:** Supervision, Writing – review & editing, Critical revision of the article, Final approval of the version to be published. **Farouk M. Okasha:** Supervision, Writing – review & editing, Critical revision of the article, Final approval of the version to be published. **Mohy S. Mansour:** Supervision, Writing – review & editing, Critical revision of the article, Final approval of the version to be published.

Conflicts of interest

None declared.

Acknowledgment

Special thanks to Prof. Mohy Mansour's research group for using some images of their work (Mansour et al., 2017, 2020) in this research article.

References

Aldén, M., Bood, J., Li, Z., Richter, M., 2011. Visualization and understanding of combustion processes using spatially and temporally resolved laser diagnostic techniques. Proc. Combust. Inst. 33, 69–97. https://doi.org/10.1016/j.proci.2010.09.004.

Bayley, A.E., Hardalupas, Y., Taylor, A.M.K.P., 2012. Local curvature measurements of a lean, partially premixed swirl-stabilised flame. Exp. Fluid 52, 963–983. https://doi.org/10.1007/s00348-011-1181-4.

Bockle, S., Kazenwadel, J., Kunzelmann, T., Shin, D.I., Schulz, C., Wolfrum, J., 2000. Simultaneous single-shot laser-based imaging of formaldehyde, OH and temperature in turbulent flames. Int. Symp. Combust. Abstr. Accept Paper 28, 29.

Boxx, I., Carter, C.D., Stöhr, M., Meier, W., 2013. Study of the mechanisms for flame stabilization in gas turbine model combustors using kHz laser diagnostics. Exp. Fluid. https://doi.org/10.1007/s00348-013-1532-4.

Cantu, L.M.L., Gallo, E.C.A., Cutler, A.D., Danehy, P.M., Johansen, C.T., Rockwell, R.D., et al., 2016. OH PLIF Visualization of a Premixed Ethylene-Fueled Dual-Mode Scramjet Combustor. 54th AIAA Aerosp Sci Meet. https://doi.org/10.2514/6.2016-1763.

Carter, C.D., Hammack, S., Lee, T., 2014. High-speed planar laser-induced fluorescence of the CH radical using the C2Σ+ - X2Π(0, 0) band. Appl. Phys. B Laser Opt. 116, 515–519. https://doi.org/10.1007/s00340-014-5899-6.

Carter, C.D., Hammack, S., Lee, T., 2016. High-speed flamefront imaging in premixed turbulent flames using planar laser-induced fluorescence of the CH C-X band. Combust. Flame 168, 66–74. https://doi.org/10.1016/j.combustflame.2016.03.024.

Comelico, V., Milan, I., 2000. Combustion analysis by image processing of premixed flames Gaetano Baldini Universith degli Studi di Milano Dipartimento di Scienze dell' Informazione. Science 80–, 708–711.

Cui, R., Qi, K., Wang, B., Wang, B., 2021. Research on large space fire monitoring based on image processing. J Phys Conf Ser. https://doi.org/10.1088/1742-6596/2074/1/012003.

Darabkhani, H.G., Oakey, J., Zhang, Y., Keshmiri, A., 2013. Study of the Flame Structure and Dynamics Using Non-intrusive Combustion Diagnostic Techniques. https://doi.org/10.2514/6.2013-2605.

Fairman, H.S., Brill, M.H., Hemmendinger, H., 1997. How the CIE 1931 color-matching functions were derived from Wright-Guild data. Color Res. Appl. 22, 11–23. https://doi.org/10.1002/(SICI)1520-6378(199702)22:1<11::AID-COL4>3.0.CO;2-7.

Fan, Q., Liu, X., Xu, L., Subash, A.A., Brackmann, C., Aldén, M., et al., 2022. Flame structure and burning velocity of ammonia/air turbulent premixed flames at high Karlovitz number conditions. Combust. Flame 238, 111943. https://doi.org/10.1016/j.combustflame.2021.111943.

Frank, J.H., Kaiser, S.A., Long, M.B., 2005. Multiscalar imaging in partially premixed jet flames with argon dilution. Combust. Flame 143, 507–523. https://doi.org/10.1016/j.combustflame.2005.08.027.

Gao, L., Yu, X., Peng, J., Tian, Y., Cao, Z., Zhong, F., et al., 2022. Flame characteristics of a cavity-based scramjet combustor using OH-PLIF and feature extraction. Int. J. Hydrogen Energy 47, 20662–20675. https://doi.org/10.1016/j.ijhydene.2022.04.172.

Gordon, R.L., Masri, A.R., Mastorakos, E., 2008. Simultaneous Rayleigh temperature, OH- and CH2O-LIF imaging of methane jets in a vitiated coflow. Combust. Flame 155, 181–195. https://doi.org/10.1016/j.combustflame.2008.07.001.

Hirsch, R., 2005. Exploring Colour Photography: a Complete Guide. Laurence King. https://books.google.com.eg/books?id=4Gx2WItWGYoC.

Izzaty, R.E., Astuti, B., Cholimah, N., 1967. Viscosity of gases. Angew. Chem. Int. Ed. 6, 951–952, 5–24.

Johansen, C.T., McRae, C.D., Danehy, P.M., Gallo, E.C.A., Cantu, L.M.L., Magnotti, G., et al., 2014. OH PLIF visualization of the UVa supersonic combustion experiment: configuration A. J. Vis. 17 (2), 131–141. https://doi.org/10.1007/s12650-014-0197-2.

Juddoo, M., Masri, A.R., 2011. High-speed OH-PLIF imaging of extinction and re-ignition in non-premixed flames with various levels of oxygenation. Combust. Flame 158 (5), 902–914. https://doi.org/10.1016/j.combustflame.2011.02.003. ISSN 0010-2180.

Kariuki, J., Dowlut, A., Yuan, R., Balachandran, R., Mastorakos, E., 2015. Heat release imaging in turbulent premixed methane-air flames close to blow-off. Proc. Combust. Inst. 35, 1443–1450. https://doi.org/10.1016/j.proci.2014.05.144.

Khalid, A., Anuar, M.D., Sies, M.F., Manshoor, B., Zaman, I., Adam, A., et al., Oct. 2014. Analysis of mixture formation and flame development in biodiesel burner combustion using direct optical visualization technique. Appl. Mech. Mater. 663, 8–12. https://doi.org/10.4028/www.scientific.net/amm.663.8. Trans Tech Publications, Ltd.

Kheirkhah, S., Gülder, O.L., 2013. Turbulent premixed combustion in V-shaped flames: characteristics of flame front. Phys. Fluids 25. https://doi.org/10.1063/1.4807073.

Kiefer, J., Li, Z.S., Zetterberg, J., Bai, X.S., Aldén, M., 2008. Investigation of local flame structures and statistics in partially premixed turbulent jet flames using simultaneous single-shot CH and OH planar laser-induced fluorescence imaging. Combust. Flame 154 (4), 802–818. https://doi.org/10.1016/j.combustflame.2008.04.002. ISSN 0010-2180.

Kim, E.K., Bae, D.K., Kim, J.H., 2015. Frequency-equivalence ratio correlation analysis of methane-air premixed flame influenced by ultrasonic standing Wave (II). J. Korean Soc. Propul. Eng. https://doi.org/10.6108/kspe.2015.19.4.045.

LaVision. Cameras for intelligent imaging (n.d.). https://www.lavision.de/en/products/cameras/. (Accessed 16 May 2023).

Li, Z.S., Li, B., Sun, Z.W., Bai, X.S., Aldén, M., 2010. Turbulence and combustion interaction: High resolution local flame front structure visualization using simultaneous single-shot PLIF imaging of CH, OH, and CH2O in a piloted premixed jet flame. Combust. Flame 157 (6), 1087–1096. https://doi.org/10.1016/j.combustflame.2010.02.017. ISSN 0010-2180.

Lomax, D.W.Z.H., Polliam, T.H., 1999. Fundamentals of Computational Fluid Dynamics. Springer, Berlin, pp. 21–47.

Mansour, M.S., Elbaz, A.M., Roberts, W.L., Senosy, M.S., Zayed, M.F., Juddoo, M., Masri, A.R., 2017. Effect of the mixing fields on the stability and structure of turbulent partially premixed flames in a concentric flow conical nozzle burner. Combust. Flame 175, 180–200. https://doi.org/10.1016/j.combustflame.2016.08.032.

Mansour, M.S., Elbaz, A.M., Roberts, W.L., Zayed, M.F., Juddoo, M., Akoush, B.M., et al., 2020. Structure and stability characteristics of turbulent planar flames with inhomogeneous jet in a concentric flow slot burner. Proc. Combust. Inst. 38, 2597–2606. https://doi.org/10.1016/j.proci.2020.06.377.

McAllister, S., Chen, J.-Y., Fernandez-Pello, A.C., 2011. Fundamentals of Combustion Processes. https://doi.org/10.1007/978-1-4419-7943-8.

Najm, H.N., Paul, P.H., Mueller, C.J., Wyckoff, P.S., 1998. On the adequacy of certain experimental observables as measurements of flame burning rate. Combust. Flame 113 (3), 312–332. https://doi.org/10.1016/S0010-2180(97)00209-5. ISSN 0010-2180.

Otsu, N., 1979. A threshold selection method from gray-level histograms. IEEE Trans. Syst. Man. Cybern. 9, 62–66.

Propane - dynamic and kinematic viscosity vs. Temperature and pressure. Eng. ToolBox. (n.d.). https://www.engineeringtoolbox.com/Propane-C3H8-dynamic-kinematic-viscosity-temperature-pressure-d_2064.html.

Shao, Y., 15 November 2007. Edge detection operators applications in flame image recognition and processing. In: Proc. SPIE Vol. 6786, MIPPR 2007: Automatic Target Recognition and Image Analysis; and Multispectral Image Acquisition, Pages 67864R. https://doi.org/10.1117/12.749874.

Skiba, A.W., Wabel, T.M., Carter, C.D., Hammack, S.D., Temme, J.E., Lee, T., Driscoll, J.F., 2017. Reaction layer visualization: a comparison of two PLIF techniques and advantages of kHz-imaging. Proc. Combust. Inst. 36, 4593–4601. https://doi.org/10.1016/j.proci.2016.07.033.

Skiba, A.W., Carter, C.D., Hammack, S.D., Lee, T., 2018a. A simplified approach to simultaneous multi-scalar imaging in turbulent flames. Combust. Flame 189, 207–211. https://doi.org/10.1016/j.combustflame.2017.10.035. ISSN 0010-2180.

Skiba, A.W., Wabel, T.M., Carter, C.D., Hammack, S.D., Temme, J.E., Driscoll, J.F., 2018b. Premixed flames subjected to extreme levels of turbulence part I: flame structure and a new measured regime diagram. Combust. Flame 189, 407–432. https://doi.org/10.1016/j.combustflame.2017.08.016.

Soika, A., Dinkelacker, F., Leipertz, A., 2003. Pressure influence on the flame front curvature of turbulent premixed flames: comparison between experiment and theory. Combust. Flame 132, 451–462. https://doi.org/10.1016/S0010-2180(02)00490-X.

Spiller, L.L., 1989. Determination of Ammonia/air diffusion coefficient using Nafion lined tube. Anal. Lett. 22, 2561–2573. https://doi.org/10.1080/00032719808052375.

Steven, D.J.D., Zumdahl, S., Zumdahl, S.A., 2000. Periodic Table of the Elements. https://doi.org/10.1016/b978-012508345-4/50002-2.

Tachtatzis, C., Lu, G., 2014. Tomographic Imaging Based Measurement of Three-Dimensional Geometric Parameters of a Burner Flame. https://doi.org/10.1109/i2mtc.2014.6860915.

Tamadonfar, P., Gülder, Ö.L., 2015. Effects of mixture composition and turbulence intensity on flame front structure and burning velocities of premixed turbulent hydrocarbon/air Bunsen flames. Combust. Flame 162, 4417–4441. https://doi.org/10.1016/j.combustflame.2015.08.009.

Tang, M.J., Shiraiwa, M., Pöschl, U., Cox, R.A., Kalberer, M., 2015. Compilation and evaluation of gas phase diffusion coefficients of reactive trace gases in the atmosphere: volume 2. Diffusivities of organic compounds, pressure-normalised mean free paths, and average Knudsen numbers for gas uptake calculations. Atmos. Chem. Phys. 15, 5585–5598. https://doi.org/10.5194/acp-15-5585-2015.

Tyagi, T., Mishra, V., 2016. 2D Gaussian filter for image processing: a study. Int. J. Sci. Technol. Eng. 3, 22–24.

Valera-Medina, A., Xiao, H., Owen-Jones, M., David, W.I.F., Bowen, P.J., 2018. Ammonia for power. Prog. Energy Combust. Sci. 69, 63–102. https://doi.org/10.1016/j.pecs.2018.07.001.

Villani, M., Aquino, P., 2020. Turbulent flame geometry measurements in a mass-production gasoline direct injection engine. Energies. https://doi.org/10.3390/en13010189.

Wabel, T.M., Skiba, A.W., Temme, J.E., Driscoll, J.F., 2017. Measurements to determine the regimes of premixed flames in extreme turbulence. Proc. Combust. Inst. 36, 1809–1816. https://doi.org/10.1016/j.proci.2016.08.065.

Wang, Q., Zhao, C., Zhang, Y., 2015. Time-resolved 3D investigation of the ignition process of a methane diffusion impinging flame. Exp. Therm. Fluid Sci. https://doi.org/10.1016/j.expthermflusci.2014.12.004.

Wang, Q., Zhang, Y., Zhao, C., 2018. Experimental investigation of coflow effect on the ignition process of a methane jet diffusion flame. Exp. Therm. Fluid Sci. https://doi.org/10.1016/j.expthermflusci.2017.10.016.

Wang, Y., Yu, Y., Zhu, X., Zhang, Z., 2020. Pattern recognition for measuring the flame stability of gas-fired combustion based on the image processing technology. Fuel 270, 117486. https://doi.org/10.1016/j.fuel.2020.117486.

Yang, L., Weng, W., Zhu, Y., He, Y., Wang, Z., Li, Z., 2020. Investigation of dilution effect on CH4/air premixed turbulent flame using OH and CH2O planar laser-induced fluorescence. Energies 13, 12–16.

Zhang, M., Wang, J., Xie, Y., Wei, Z., Jin, W., Huang, Z., Kobayashi, H., 2014. Measurement on instantaneous flame front structure of turbulent premixed CH4/H2/air flames. Exp. Therm. Fluid Sci. 52, 288–296. https://doi.org/10.1016/j.expthermflusci.2013.10.002.